

Super-cluster simulations: impact of baryons on the matter power spectrum and weak lensing forecasts for Super-CLASS

Aaron Peters,^{1*} Michael L. Brown,¹ Scott T. Kay¹ and David J. Barnes¹

¹*Jodrell Bank Centre for Astrophysics, School of Physics and Astronomy, The University of Manchester, Manchester M13 9PL*

Accepted XXX. Received YYY; in original form ZZZ

ABSTRACT

We use a combination of full hydrodynamic and dark matter only simulations to investigate the effect that baryonic physics and selecting super-cluster regions have on the matter power spectrum, by re-simulating a sample of super-cluster sub-volumes. On large scales we find that the matter power spectrum measured from our super-cluster sample has at least twice as much power as that measured from our random sample. Our investigation of the effect of baryonic physics on the matter power spectrum is found to be in agreement with previous studies and is weaker than the selection effect over the majority of scales. In addition, we investigate the effect of targeting a cosmologically non-representative, super-cluster region of the sky on the weak lensing shear power spectrum. We do this by generating shear and convergence maps using a line of sight integration technique, which intercepts our random and super-cluster sub-volumes. We find the convergence power spectrum measured from our super-cluster sample has a larger amplitude than that measured from the random sample at all scales. We frame our results within the context of the Super-CLuster Assisted Shear Survey (Super-CLASS), which aims to measure the cosmic shear signal in the radio band by targeting a region of the sky that contains five Abell clusters. Assuming the Super-CLASS survey will have a source density of 1.5 galaxies/arcmin², we forecast a detection significance of $2.7^{+1.5}_{-1.2}$, which indicates that in the absence of systematics the Super-CLASS project could make a cosmic shear detection with radio data alone.

Key words: large-scale structure of Universe, galaxy: formation, gravitational lensing: weak, methods: numerical, clusters: general

1 INTRODUCTION

Light from background source galaxies propagating through the Universe gets deflected by inhomogeneities in the matter distribution. This phenomenon, termed weak gravitational lensing, causes coherent distortions, typically percent level, to both the size (convergence) and shape (shear) of source galaxies (for reviews see, [Bartelmann & Schneider 2001](#); [Schneider 2005](#); [Hoekstra & Jain 2008](#)). Weak gravitational lensing, when applied to studies of the large scale structure of the Universe, is known as cosmic shear and can be directly related to the matter power spectrum ([Kaiser 1992](#)).

Cosmic shear measurements have been successfully used to constrain cosmological parameters in various surveys (some recent results include e.g. [Fu et al. 2008](#); [Jee et al. 2013](#); [Benjamin et al. 2013](#); [Kilbinger et al. 2013](#); [Heymans](#)

[et al. 2013](#); [Fu et al. 2014](#); [Abbott et al. 2016](#); [Hildebrandt et al. 2016](#)), and are believed to hold the most promise for probing dark energy. In addition, some of the most accurate constraints on the matter power spectrum come from weak lensing, particularly in the non-linear regime. The next stage of optical weak lensing surveys, e.g. the ground based Large Synoptic Survey Telescope¹ (LSST) or the space mission Euclid², are expected to observe two orders of magnitude more source galaxies than completed weak lensing surveys. As a result, this decrease in statistical uncertainty brings about the difficult task of reducing the systematic uncertainties by an order of magnitude. Due to the statistical errors currently present in lensing, analytic models based on simulations which assume that baryons trace dark matter

* Contact email: aaron.peters@postgrad.manchester.ac.uk

¹ <http://www.lsst.org/lsst/>

² <http://sci.esa.int/euclid/>

particles perfectly, i.e., dark matter only simulations, have been sufficient.

However, to take full advantage of future surveys, the accuracy with which we model the matter power spectrum will have to be improved to the few percent level. As a result we must include baryonic processes, such as star formation, radiative cooling, supernovae feedback and active galactic nuclei (AGN) feedback. Cooling gas has been found to cluster on smaller scales than dark matter, which means the matter power spectrum is under-predicted in dark matter only simulations on scales greater than $k \sim 6h/\text{Mpc}$ (e.g., [Jing et al. 2006](#); [Rudd et al. 2008](#); [Guillet et al. 2010](#); [Casarini et al. 2011](#); [van Daalen et al. 2011](#)). Additionally, [van Daalen et al. \(2011\)](#) found that matter power spectra measured in hydrodynamic simulations that model AGN feedback were suppressed on intermediate scales, when compared to dark matter only simulations. In a follow up paper ([Semboloni et al. 2011](#)), the effect of baryons on the matter power spectrum, when used as part of a cosmic shear study, was found to significantly bias cosmological parameter estimation.

In addition, systematic effects can be reduced by performing multi wavelength weak lensing investigations ([Demetroullas & Brown 2016](#)). Particularly, performing weak lensing studies in the radio band provides a unique opportunity to reduce, e.g., systematics due to the point spread function and intrinsic galaxy alignments ([Brown & Battye 2011](#)). The smaller fields of view, lower effective source densities and limited resolution presently available mean the optical waveband is favoured for lensing surveys. However, with the upcoming arrival of wide area radio surveys, such as the Square Kilometre Array (SKA³), this will change ([Brown et al. 2015](#); [Harrison et al. 2016](#); [Bonaldi et al. 2016](#)). The Super-CLuster Assisted Shear Survey’s (Super-CLASS⁴) principal science goal is to measure the cosmic shear signal, while further developing techniques for analysing radio weak lensing data.

In order to maximise the cosmic shear signal measured, Super-CLASS targets a region of the sky known to contain a super-cluster made up of five Abell clusters. Observations of super-cluster fields from the COMBO-17 ([Gray et al. 2002](#)) and STAGES HST surveys ([Heymans et al. 2008](#)), used weak lensing analysis to probe the dark matter distribution of the Abell 901/902 super-cluster. In addition, [Brown et al. \(2003\)](#) found the shear power spectrum measured from the Abell 901/902 super-cluster field had an amplitude significantly higher than that measured in random fields.

We know small super-cluster fields are not cosmologically representative regions of the sky, which implies weak lensing measurements are going to be affected when selecting a super-cluster field as opposed to a random field. In this paper we intend to quantify this effect, hereafter referred to as the ‘selection effect’, as well as the effect of baryonic physics on the matter power spectrum. We do this by selecting a sample of 61 super-cluster sub-volumes that meet criteria specifically chosen to mimic the five Abell clusters targeted by the Super-CLASS survey, along with a sample of 60 random sub-volumes, from a large volume dark matter only simulation. The sub-volumes in these two samples are

re-simulated using the zoomed re-simulation technique at a higher resolution and with full gas physics. With these re-simulations we are able to compare the difference between measuring the matter power spectrum in random and super-cluster sub-volumes. In addition, we investigate how the matter power spectrum is affected by baryonic physics, and which of the two effects is dominant. We also generate shear and convergence maps using a line of sight integration technique, which intercept the random and supercluster sub-volumes at $z = 0.24$, approximately matching the Super-CLASS super-cluster redshift. These are then used to study the difference between the shear power spectrum measured by a weak lensing survey that targets a random patch of the sky as opposed to one containing a super-cluster.

The outline of this paper is as follows. We discuss the simulations used for this work and the identification method employed to select a sample of super-cluster sub-volumes, in Section 2. In Section 3 we examine how the selection effect will affect the matter power spectrum (Section 3.1), we investigate how baryonic process affect the matter power spectrum (Section 3.2), and we also compare the effect of baryonic physics on the matter power spectrum to that of selection (Section 3.3). In Section 4 we detail the line of sight integration technique used to generate convergence and shear maps (Section 4.1), the effect of selection on the shear and convergence power spectra (Section 4.2) and lastly we forecast the constraining power of the Super-CLASS survey (Section 4.3). Finally, we conclude by summarising our results in Section 5.

2 SIMULATIONS

In the following section we describe the large dark matter only simulation we used, hereafter referred to as the ‘parent’ simulation. Additionally, we detail the selection criteria used to identify the super-cluster sample and the baryonic physics implemented when we re-simulated the sample sub-volumes with the zoom technique.

2.1 Parent Simulation

A simulation with a very large cosmologically representative volume, of several Gpc^3 , is necessary to simulate the large population of massive clusters that we require to find a sample of super-clusters. To investigate the effect of baryons in super-cluster regions we require high resolution hydrodynamic simulations with volumes that are sufficiently large to produce the large scale power needed for a sample of super-clusters to be identified. Computational resources restrict our ability to simulate hydrodynamical volumes of this magnitude to a sufficiently high resolution given the gas physics we wish to implement. However, we can apply a workaround called the zoomed re-simulation technique ([Katz & White 1993](#); [Tormen et al. 1997](#)), where a sub-volume of a larger dark matter only simulation is re-simulated at higher resolution. We will use this technique to re-simulate sub-volumes of the parent simulation for our matter power spectrum investigation. In addition, the large volume of the parent simulation was needed for the weak lensing analysis, to generate the shear and convergence maps along light-cones through the simulation.

³ <https://www.skatelescope.org/>

⁴ <http://www.e-merlin.ac.uk/legacy/projects/superclass.html>

Table 1. Key observational properties of the five Abell clusters in the Super-CLASS field. Luminosities are taken from the BAX database (Sadat et al. 2004), while the positions on the sky and redshifts are taken from Briel & Henry (1993). Masses are estimated from the $L_x - M_{500}$ relation (see text for details).

Cluster Name	RA 1950	DEC 1950	z	L_x [0.1–2.4]keV	M_{500}
Abell 968	10 17 44.1	68 36 34	0.195	0.401×10^{44} erg/s	$(1.2 \pm 0.3) \times 10^{14} M_\odot$
Abell 981	10 20 36.0	68 20 06	0.201	1.670×10^{44} erg/s	$(2.7 \pm 0.7) \times 10^{14} M_\odot$
Abell 998	10 22 47.8	68 11 13	0.203	0.411×10^{44} erg/s	$(1.2 \pm 0.3) \times 10^{14} M_\odot$
Abell 1005	10 23 40.0	68 27 18	0.200	0.268×10^{44} erg/s	$(1.0 \pm 0.2) \times 10^{14} M_\odot$
Abell 1006	10 24 10.7	67 17 44	0.204	1.320×10^{44} erg/s	$(2.4 \pm 0.6) \times 10^{14} M_\odot$

The parent simulation is a large periodic dark matter only simulation with a cubic volume of $(3.2 \text{ Gpc})^3$, which we used to select our sample of super-clusters. It follows the evolution of 2520^3 dark matter particles, each of mass $5.43 \times 10^{10} M_\odot/h$, from $z = 127$ to $z = 0$. The comoving gravitational softening length of the parent simulation is $40 \text{ kpc}/h$. The simulation was run using the GADGET-3 code (Springel et al. 2008), an updated and more efficient version of the publicly available GADGET-2 code (Springel 2005).

The initial conditions were created by first generating a glass like particle distribution (White 1994), then each particle’s displacement and velocity were calculated according to second order perturbation theory using the method laid out in Jenkins (2010), using the public Gaussian white noise field PANPHASIA (Jenkins 2013; Jenkins & Booth 2013). Its cosmological parameters $[\Omega_m, \Omega_\Lambda, \Omega_b, h, \sigma_8, n_s, Y] = [0.307, 0.693, 0.04825, 0.6777, 0.8288, 0.9611, 0.248]$, were chosen to be consistent with Planck year 1 results (Planck Collaboration et al. 2014).

2.2 Supercluster Identification

Here we detail the method used to identify a sample of super-cluster sub-volumes within the parent simulation. As our aim is to identify super-cluster sub-volumes with properties that best resemble the five Abell clusters in the Super-CLASS field, we begin with a brief description of this.

The Super-CLASS project is a deep field, radio weak lensing survey. The project’s primary science goal is to detect a cosmic shear signal by targeting a region of sky containing a super-cluster. Specifically, the one square degree, Super-CLASS field contains five known, $z \sim 0.2$ Abell clusters (A968, A981, A998, A1005, A1006). We detail in Table 1 some of their observational properties. The positions on the sky and redshifts were taken from Briel & Henry (1993), while the X-ray luminosities were taken from the BAX database (Sadat et al. 2004). Pratt et al. (2009) investigated X-ray luminosity scaling relations for a sample of 33 local ($z < 0.2$) galaxy clusters from REXCESS. We determined the M_{500}^5 masses listed in the final column of Table 1 using the following relation from the aforementioned paper

$$M_{500} = \left(\frac{L_x}{L_0} h(z)^{-7/3} \right)^{1/\alpha} M_0, \quad (1)$$

where $h^2(z) = \Omega_m(1+z)^3 + \Omega_\Lambda$. The values of the constants

⁵ We define M_{500} as the mass enclosed within a sphere of radius R_{500} , in which the mean density is five hundred times that of the critical density of the Universe.

for luminosities L_x measured in the [0.1–2.4] keV band are as follows, $L_0 = 0.78 \pm 0.07 \times 10^{44}$ erg/s, $\alpha = 1.83 \pm 0.14$ and $M_0 = 2 \times 10^{14} M_\odot$.

To select similar regions in the simulation, we first identified clusters at the snapshot that corresponds to $z = 0.24$, the closest available redshift. Halo structures were identified using the *Friends-of-Friends* (FOF, Davis et al. 1985) algorithm on particles, choosing a linking length of $b = 0.2$ times the mean inter-particle separation. To separate the FOF halo structures into self bound substructures the SUBFIND algorithm (Springel et al. 2001; Dolag et al. 2009) was applied. Finally, the *spherical overdensity* algorithm (SO, Lacey & Cole 1994) was applied to each of the SUBFIND haloes, to calculate the spherical overdensity radii and masses.

The criteria listed below were chosen to select a sample of sub-volumes in the parent simulation, that contain super-clusters with properties that best resemble the five Abell clusters contained in the Super-CLASS field. To identify these regions we ran the FOF algorithm on haloes, rather than particles.

(i) The FOF algorithm was only used on haloes that fell in the cluster mass range, $(0.5 \leq M_{500} \leq 5) \times 10^{14} M_\odot/h$. Our mass range was based on the estimated masses of the Abell clusters, shown in Table 1.

(ii) The FOF linking length l , was chosen to approximately equal the mean projected comoving distance separating the five Abell clusters. Rounding to the nearest integer, the linking length was determined to be $l = 8 \text{ Mpc}/h$.

(iii) After using the FOF algorithm as stated we selected the super-clusters that contained exactly 5 clusters. We identified 61 super-clusters, each containing five cluster members that fall in the mass range $(0.5 \leq M_{500} \leq 5) \times 10^{14} M_\odot/h$ and all of which are within $8 \text{ Mpc}/h$ of at least one other member.

Finally, the minimum side length of a cube that could be drawn about any super-cluster’s centre of mass and guarantee the enclosure of all five respective clusters was determined as follows. The bottom left panel of Fig. 1 shows a two dimensional mass projection of the gas in the super-cluster which has the largest distance d between its centre of mass and that of its furthest cluster, projected along one of the x, y, z axes. Assuming a cluster is completely enclosed by a sphere of radius $3r_{200}$ about its centre of mass, a cube drawn about the super-cluster’s centre of mass with a side length of $2(d + 3r_{200})$ will enclose all member clusters completely. This was found to be $40.16 \text{ Mpc}/h$ for the super-cluster shown in Fig. 1 and, being the most extreme case, was used for the rest of the sample to guarantee their respective enclosure.

For comparison purposes and to quantify the enhance-

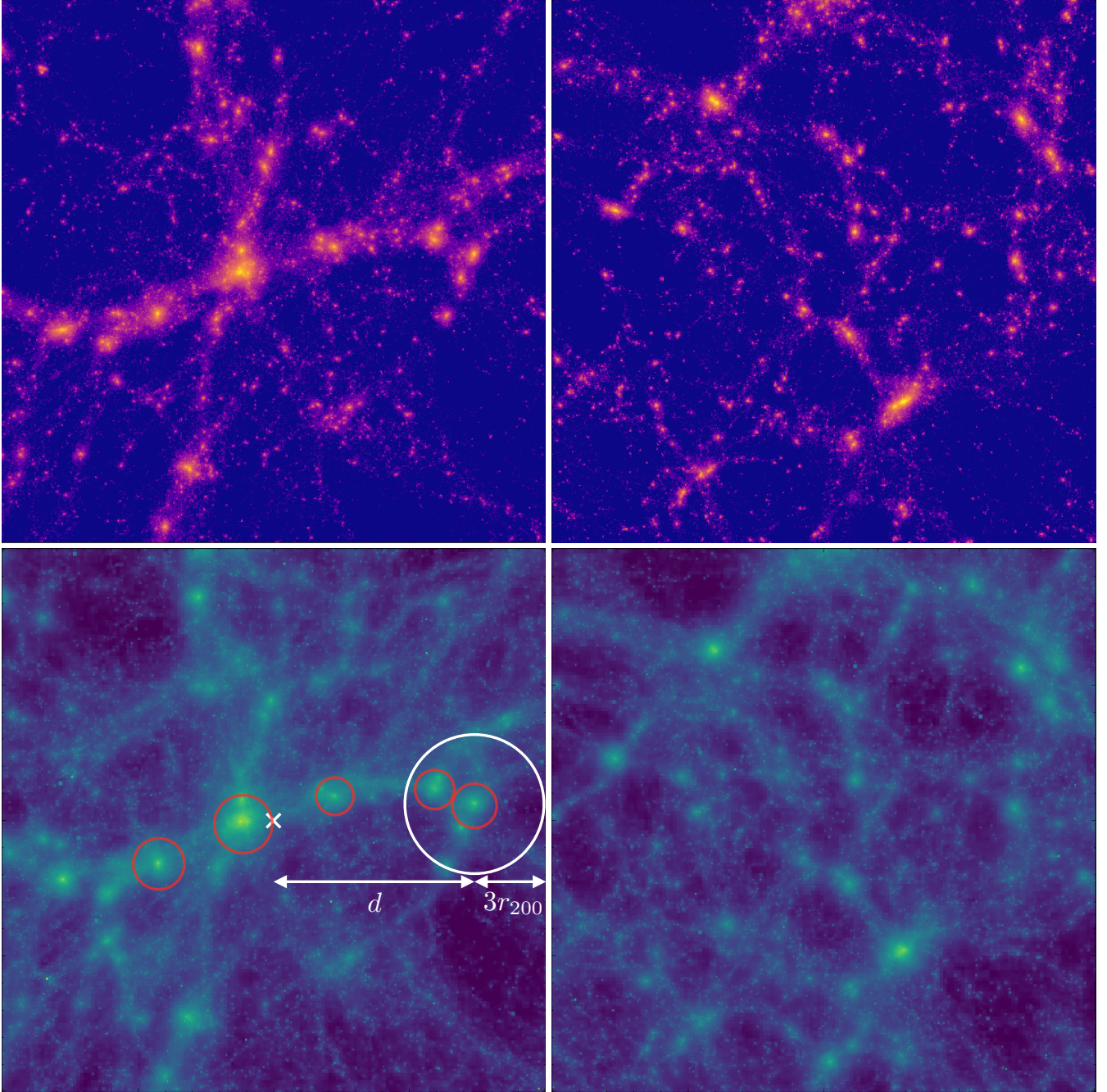


Figure 1. Example of the two dimensional surface mass projection for one super-cluster sub-volume in the left two panels and one random sub-volume in the right two panels. The surface mass projections of the dark matter and gas are shown in the top and bottom panels respectively. The cross in the centre of the bottom left panel is the super-cluster’s centre of mass, the 5 red circles enclose the 5 cluster’s centre of mass and the white circle with a radius of $3r_{200}$ is drawn about the centre of mass of a particular member cluster. The distance projected along an axis from the centre of mass of the circled cluster to the centre of mass of the super-cluster, d , is the longest of any cluster in our super-cluster sample (see text for details).

ment of the power spectrum in super-cluster regions, we also randomly selected 60 additional cubic sub-volumes from the parent simulation. These sub-volumes were used as a control sample and like the super-cluster sub-volumes also have a side length of $40.16 \text{ Mpc}/h$. Hereafter, we will refer to them as the random sample. An example of one of these sub-volumes’ is also shown in the right panels of Fig. 1.

2.3 Zoomed Re-simulations

In this section we describe the zoomed re-simulation technique that we used to re-simulate our sample of random and super-cluster sub-volumes of the parent simulation. These re-simulations are part of the Virgo consortium’s Massive Clusters and Intercluster Structures (MACSIS) project

(Barnes et al. 2017; Henson et al. 2016), which extends the BArYons and HALoes of MAssive Systems (BAHAMAS) (McCarthy et al. 2016) simulation to more massive clusters.

While the aim of this study is different, we used the same method employed in the MACSIS project to re-simulate the sub-volumes of interest. For every member of the random and super-cluster samples we used the BAHAMAS code to perform both dark matter only and hydrodynamical re-simulations, using the same cosmological parameters. The resolution of the initial conditions were reduced throughout the parent simulation except for the sub-volume of interest, where they were enhanced. This means on re-simulation, the large scale power of the parent simulation was preserved and the region of interest was simulated at a sufficiently high resolution.

To re-simulate the sub-volumes we used a heavily modified version of the Tree-PM, smooth particle hydrodynamical code GADGET-3, that was developed to include subgrid physics in the suite of simulations used in the OWLS project (Schaye et al. 2010). Some of the subgrid prescriptions included are star formation (Schaye & Dalla Vecchia 2008), radiative cooling (Wiersma et al. 2009), feedback from supernovae (Dalla Vecchia & Schaye 2008) and AGN (Booth & Schaye 2009). McCarthy et al. (2016) showed that by calibrating the subgrid model of feedback to a small number of observables, the BAHAMAS simulation was able to reproduce the observed stellar and gas content of massive systems.

We performed dark matter only (DMO) re-simulations with a particle mass of $5.2 \times 10^9 M_\odot/h$ and hydrodynamical (HYDRO) re-simulations with a dark matter particle mass of $4.4 \times 10^9 M_\odot/h$ and an initial gas particle mass of $8.0 \times 10^8 M_\odot/h$, for every member of the random and super-cluster samples. Below $z = 3$ the gravitational softening length of the high resolution particles were set to 4 kpc/h in physical co-ordinates, whilst for $z > 3$ they were set to 16 kpc/h in co-moving co-ordinates.

In Fig. 2 we show how the hot gas fraction f_{gas} , measured within R_{500} , depends on their M_{500} . We calculate f_{gas} by dividing the total mass of the gas with temperature above $10^{5.2}$ K, which we would expect to be emitting X-rays, by the total mass of all matter within a radius of R_{500} from the centre of the cluster. The yellow curve is the median f_{gas} for clusters in the BAHAMAS sample, while the blue curve is that taken from our super-cluster sample. The shaded area surrounding the yellow and blue curves represent the region between their 16th and 84th percentiles. We were unable to bin the massive clusters from our random sample due to limited numbers, they are instead shown as red dots. Similarly, the high mass bin for the super-cluster sample was removed from the plot as it only consisted of 3 clusters. The slight discrepancy, between the median curves of the BAHAMAS and super-cluster samples, could be due to the fact that BAHAMAS uses a slightly different cosmology. Multiplying f_{gas} by the universal gas fraction is not necessarily sufficient to correct for this effect. However, the more likely cause is the fact that the majority of our clusters are situated in overdense super-cluster regions. These overdense regions would most likely make it harder for the gas heated by stars and AGN to escape, which would result in increased gas fractions in our clusters (this is consistent with our findings below, in Fig. 7).

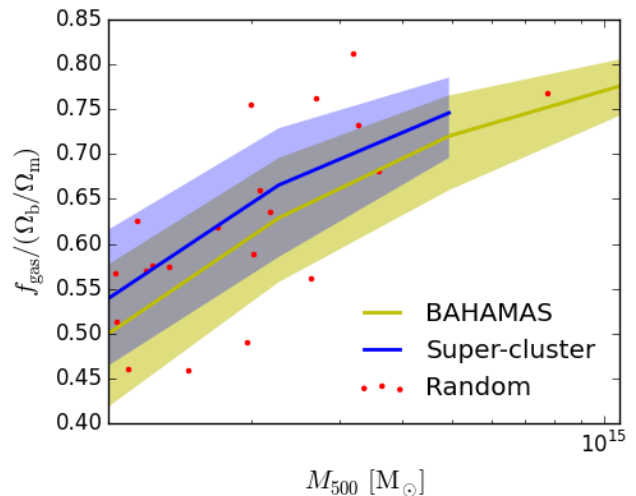


Figure 2. Comparison of the median $f_{\text{gas}} - M_{500}$ relation for clusters from the BAHAMAS sample to the clusters contained in our super-cluster sub-volumes, shown in yellow and blue respectively. The shaded area surrounding the yellow and blue curves represent the region between their 16th and 84th percentiles. We were unable to bin the limited number of massive clusters in our random sample, they are instead shown as red dots. In addition the high mass bin of the super-cluster sample has been removed, as it only consisted of 3 clusters.

3 3D MATTER POWER SPECTRUM

In this section we will present the matter power spectrum estimates measured from our simulations. First, we will investigate the selection effect (introduced by specifically targeting super-cluster regions) by comparing the matter power spectrum measured from our random sub-volumes to those of our super-cluster sub-volumes. Then we study the effect of baryonic physics on the matter power spectrum, before examining which of these effects, selection or baryons, is more important.

In order to describe fluctuations in the matter density $\rho(\mathbf{x}, t)$, at comoving position \mathbf{x} , and time t , it is convenient to use the overdensity

$$\delta(\mathbf{x}, t) = \frac{\rho(\mathbf{x}, t)}{\bar{\rho}(t)} - 1, \quad (2)$$

where $\bar{\rho}(t)$ is the background density of the Universe. The overdensity has the range, $-1 \leq \delta < \infty$, with $-1 \leq \delta < 0$ corresponding to underdense regions and $0 < \delta$ corresponding to overdense regions. Expanding the overdensity field $\delta(\mathbf{x})$ in terms of Fourier components, in a large box of comoving volume V we can represent the overdensity field such that

$$\delta(\mathbf{x}) = \frac{V}{(2\pi)^3} \int_V \delta_{\mathbf{k}} \exp(i\mathbf{k} \cdot \mathbf{x}) d^3k, \quad (3)$$

where \mathbf{k} is the comoving wavenumber. The Fourier components can be expressed in terms of an amplitude $|\delta_{\mathbf{k}}|$, and phase $\phi_{\mathbf{k}}$ such that $\delta_{\mathbf{k}} = |\delta_{\mathbf{k}}| \exp(i\phi_{\mathbf{k}})$.

The overdensity field $\delta(\mathbf{x})$ can be approximated as Gaussian whilst in the linear regime, when the phases and amplitudes of the Fourier components are independent. The full statistical properties of a homogenous, isotropic Gaussian random field are described by the power spectrum $P(k)$,

defined to be $\langle |\delta_{\mathbf{k}}|^2 \rangle$, where we take the average over all possible spatial orientations. Note that the power spectrum depends only on the modulus of the wavenumber \mathbf{k} and not its orientation.

Throughout this paper we used the publicly available code POWMES⁶ (Colombi et al. 2009) to measure the matter power spectrum from our simulations. POWMES estimates the particle distribution’s Fourier modes, using a Taylor expansion on the cosine and sine transforms. The accuracy of the Fourier transform increases by using higher order approximations of the Taylor expansion, taking into account small displacements within grid cells. For a more detailed description of the code see Colombi et al. (2009).

Unless stated otherwise, all matter power spectra estimates in this paper were measured from the snapshot corresponding to $z = 0.24$, to mimic the properties of the Abell clusters in the Super-CLASS field. In addition, we found that the shot noise due to the discreteness of particles in the DMO and HYDRO sub-volumes does not begin to bias matter power spectrum measurements until $k > 70 h/\text{Mpc}$. As a result, we do not discuss any matter power spectra measurements for wavenumbers higher than $k = 70 h/\text{Mpc}$.

We note that a complication arises when the matter power spectrum is measured within a sub-volume of a simulation due to an incomplete sampling of fluctuations. Modes with wavelengths larger than typical sub-volume scales, super-sample modes, observably impact how sub-sample modes evolve through nonlinear mode coupling. Hamilton et al. (2006) originally pointed out the super-sample effect on the covariance of the power spectrum, where it was referred to as beat coupling. The super-sample effect vanishes when measuring the power spectrum throughout the entire volume of a simulation due to periodic boundary conditions. Takahashi et al. (2009) found that the measured power spectrum in comparison to the truth is biased low at wavenumbers corresponding to the sub-volume’s side length, $k \sim 1/L_n$, but reduces progressively as the scales decrease, $k \gg 1/L_n$. Although, the super-sample effect does bias our matter power spectrum estimates, our results comparing one power spectrum with another will not be affected (i.e. the super-sample effect biases all of our estimates in the same way). The super-sample effect is less of an issue for our shear power spectrum analysis in section 4 (and observationally), where large scale modes along the line of sight are included.

3.1 Effect of Super-Cluster Selection on the Matter Power Spectrum

In this section we investigate how the overdensity of a region affects the matter power spectrum measured from that region’s sub-volume. We examine this selection effect on the matter power spectra by comparing the matter power spectra measured from our random and super-cluster samples.

In Fig. 3, we plot the median matter power spectrum for the super-cluster DMO sub-volumes and that of the random DMO sub-volumes, both divided by the median matter power spectrum for the random DMO sub-volumes. Therefore, any deviation from unity is due to the effect of selection on the power spectrum. The shaded area surrounding

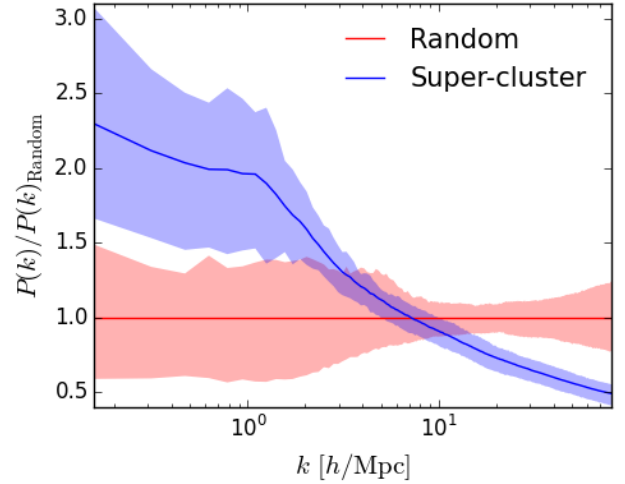


Figure 3. The median power spectra of the super-cluster and random samples measured from the DMO re-simulations, both divided by the median power spectrum of the DMO random sample. The ratio for the super-cluster and random sample is shown in blue and red respectively, and the shaded area surrounding the curves represent the region between their 16th and 84th percentiles.

the blue and red curves represent the region between the super-cluster and random samples’ 16th and 84th percentiles, which shows the scatter in the power spectra of the samples.

On large scales, $k \leq 1 h/\text{Mpc}$, the super-cluster sample has more than twice the power of the random sample on average. As we move to smaller scales the excess power in the super-cluster sub-volumes begins to decline and beyond $k \sim 7 h/\text{Mpc}$, comparatively, the power of the random sample begins to dominate. On the smallest scales measured, $k \sim 70 h/\text{Mpc}$, the random sample now has double the power of the super-cluster sample.

We note that the mean overdensity measured within the sub-volumes of our super-cluster and random samples are approximately one and zero respectively. The extra power seen in the super-cluster sample on large scales is expected. Chiang et al. (2014) showed that a correlation exists between the matter power spectrum measured in a sub-volume and the overdensity of that sub-volume, with the more overdense sub-volumes having more power over the scales which they studied, $k \leq 1 h/\text{Mpc}$. To further investigate the effect of selection on the matter power spectrum we look at the individual sub-volumes of our two samples.

In Fig. 4 we show, at two different scales, how the matter power spectrum measured in each DMO sub-volume varies with overdensity. In the top panel we plot the dependence of the amplitude of the matter power spectrum, at $k_1 = 1 h/\text{Mpc}$, versus overdensity. In red are the random sub-volumes and in blue the super-cluster sub-volumes. With the exception of one outlier from the random sample, it can be seen that the power measured within a sub-volume increases with its overdensity, in agreement with Chiang et al. (2014).

The equivalent plot for a smaller scale, $k_2 = 50 h/\text{Mpc}$, is shown in the bottom panel. We see a tighter correlation in the opposite direction, with more overdense sub-volumes having less power than their underdense counterparts. We found the same correlation at small scales in the HYDRO

⁶ <http://www.projet-horizon.fr/article345.html>

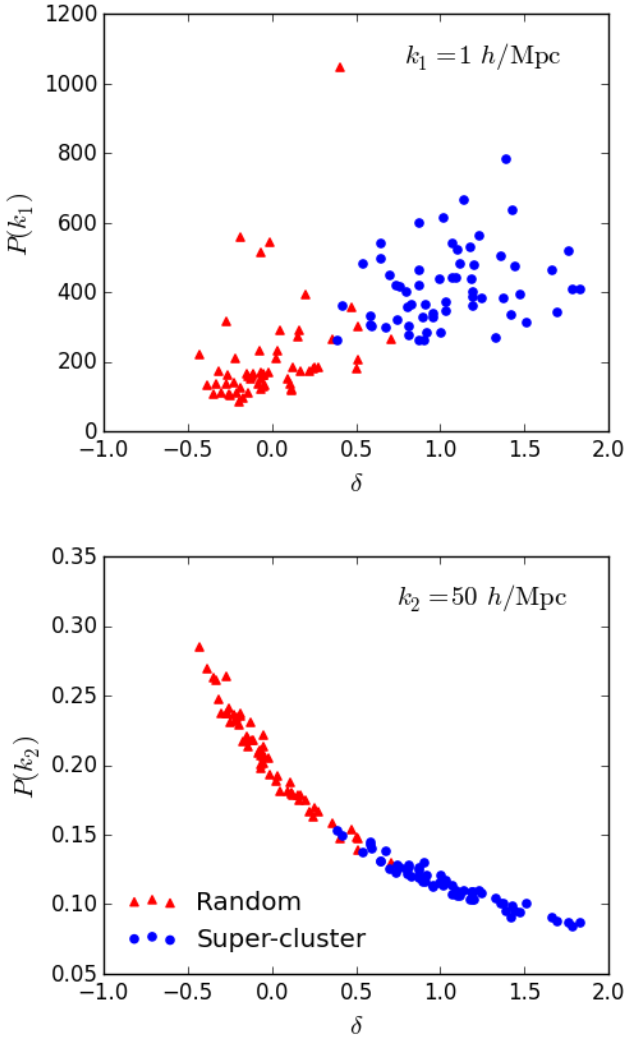


Figure 4. The dependence of the amplitude of the matter power spectrum on the overdensity of the sub-volumes from which it was measured. All 121 sub-volumes are shown, the super-cluster sample in blue and the random sample in red. The top and bottom panels show the correlation at scales corresponding to $k_1 = 1 h/\text{Mpc}$ and $k_2 = 50 h/\text{Mpc}$ respectively.

re-simulated sub-volumes and the original sub-volumes of the parent simulation for $k \geq 10 h/\text{Mpc}$, which indicates this is not a resolution artefact. Halo assembly bias perhaps provides a plausible explanation for this effect. Dalal et al. (2008) found that low mass halos in overdense regions are biased low, i.e. as the background density is raised, the number of low mass peaks are reduced as they are converted to high mass peaks. Another process that may contribute to the observed anti correlation is tidal stripping. In the more overdense regions these low mass halos are more likely to be in the presence of clusters, which could potentially strip these cluster galaxies of their mass.

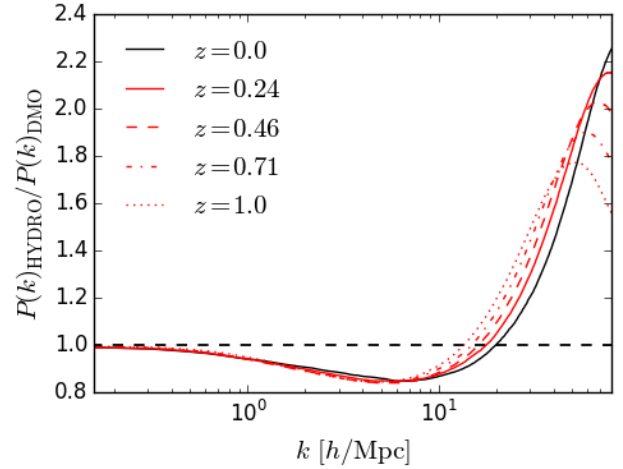


Figure 5. The median of the random sample’s matter power spectra measured from the HYDRO re-simulations divided by that of their DMO counterparts. The ratios measured at $z = 0.0, 0.24, 0.46, 0.71$ and 1.0 are represented by the solid black, solid red, dashed red, dash-dotted red and dotted red curves respectively.

3.2 Effect of Baryons on the Matter Power Spectrum

In this section we investigate the effect of baryons on the matter power spectrum by comparing the matter power spectra measured from our HYDRO re-simulations with those of our DMO re-simulations.

Plotted in Fig. 5 is the median of the matter power spectra measured from the HYDRO re-simulations divided by the matter power spectrum measured from their DMO counterparts, in our random sample. As the initial conditions of the HYDRO and DMO re-simulations are the same for a particular sub-volume, any deviation from unity results directly from the various effects of the baryonic physics present. The power spectra were measured at redshifts $z = 0.0, 0.24, 0.46, 0.71$ and 1.0 and their ratios are represented by the solid black, solid red, dashed red, dash-dotted red and dotted red curves respectively. There is no effect on the matter power spectrum due to baryons on the largest scales but they suppress the power on intermediate scales, $k \sim 0.3 - 10 h/\text{Mpc}$, and boost the power on small scales. Note this effect does not depend strongly on redshift.

Our results are broadly consistent with previous work. van Daalen et al. (2011) compared three different hydrodynamical simulations to a reference dark matter only simulation, all of which were given the same initial conditions. Our simulations are most similar to their AGN model, which has baryonic processes that best resemble ours. They attributed the increase in power at the small scales to cooling baryons falling into potential wells, while at intermediate scales $k \sim 1 - 10 h/\text{Mpc}$ they showed the suppression of power was due to AGN feedback removing baryons from halos. On the largest scales, there is little to no effect on the power spectrum that results from baryons because the baryons are expected to trace of the dark matter on adequately large scales.

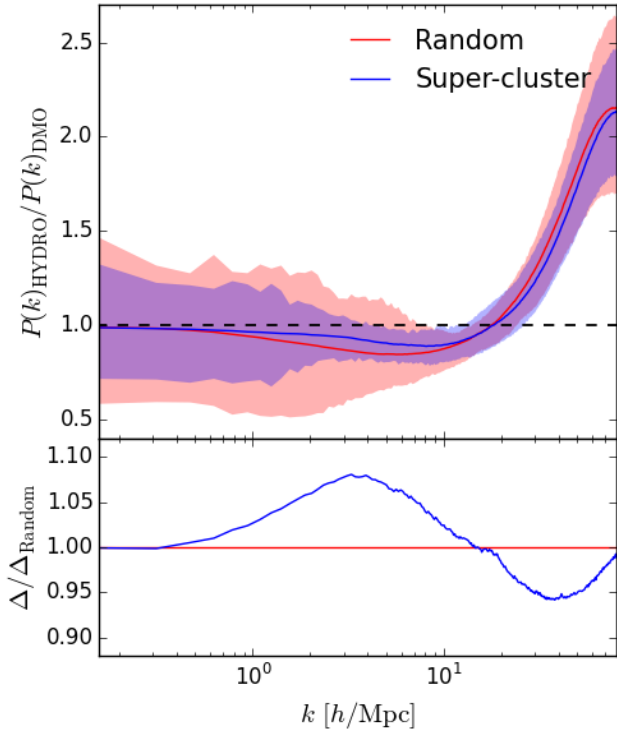


Figure 6. The top panel shows the median of the matter power spectra measured in the HYDRO re-simulations divided by that of their DMO counterparts, for the random and super-cluster samples in red and blue respectively. The shaded area surrounding the curves represent the region between their 16th and 84th percentiles. The bottom panel shows the super-cluster ratio divided by the random ratio.

We can examine in more detail the effect baryons have on the matter power spectrum by comparing its effect on the super-cluster sample to that on the random sample. In the top panel of Fig. 6 we plot the median matter power spectrum measured in the HYDRO samples divided by that of the DMO samples. The red and blue curves represent the random and super-cluster HYDRO/DMO samples respectively and again the shaded area surrounding the curves represent the region between their 16th and 84th percentiles. On intermediate scales, $k \sim 1 - 10 h/\text{Mpc}$, the effect of baryons in the random sample suppresses the power of the HYDRO power spectrum to as little as 83% of the DMO power spectrum. In comparison, the super-cluster sample’s HYDRO power spectrum is suppressed to 88% of the DMO power spectrum.

The differences are shown more clearly in the bottom panel, where the HYDRO/DMO power spectrum of the super-cluster sample is divided by that of the random sample. The suppression of the matter power spectrum due to the effect of baryons can be seen to be stronger by several percent in the random sample. At small scales, beyond $k \sim 20 h/\text{Mpc}$, the boost in power due to baryons in the super-cluster sample is weaker than the boost in power due to baryons in the random sample. In short, at both intermediate and small scales, the effect of baryons on the matter

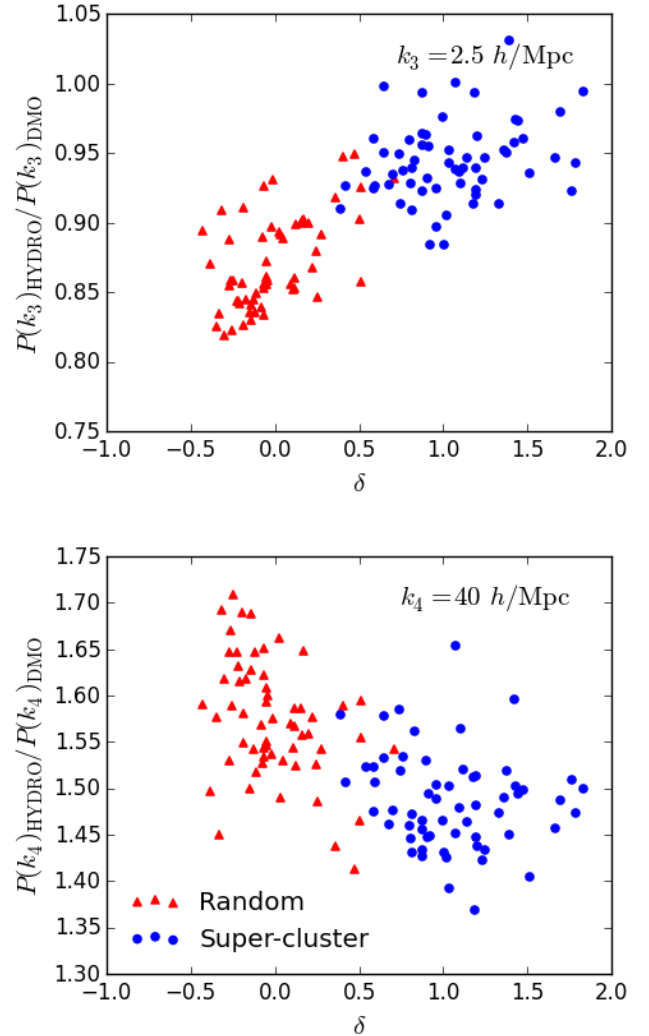


Figure 7. The dependence of the HYDRO/DMO matter power spectrum ratio (effect of baryons) on the overdensity of the sub-volumes from which they are measured. All 121 sub-volumes are shown, the super-cluster sample in blue and the random sample in red. The top and bottom panels show the correlation at scales corresponding to $k_3 = 2.5 h/\text{Mpc}$ and $k_4 = 40 h/\text{Mpc}$ respectively.

power spectrum in the super-cluster sample is less severe than in the random sample.

Similar to Fig. 4 we can also demonstrate how the effect of baryons is dependent on the overdensity of the sub-volume. In Fig. 7 we show how the HYDRO/DMO matter power spectra ratio in each sub-volume varies with its overdensity, at two different scales. The wavenumbers k_3 and k_4 were chosen to correspond to the peak and trough in the bottom panel of Fig. 6. In red are the random sub-volumes and in blue the super-cluster sub-volumes. In the top panel we plot the dependence of this ratio on the overdensity, measured at intermediate scales, $k_3 = 2.5 h/\text{Mpc}$. Generally speaking, the higher the overdensity of a sub-volume the less the power is suppressed by baryons. A plausible explanation is that on these scales, the AGN feedback becomes

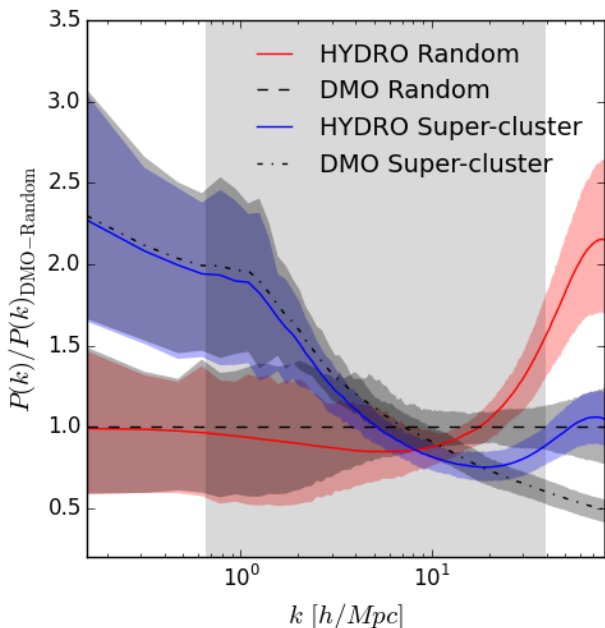


Figure 8. The ratios of the median matter power spectrum measured from a sample and the median matter power spectrum measured in the random sample’s DMO re-simulations. The ratio for the HYDRO supercluster sample, DMO supercluster sample, HYDRO random sample and DMO random sample are shown in solid blue, black dash-dotted, solid red and black dashed respectively. The shaded area surrounding the curves represent, the region between their 16th and 84th percentiles. The grey shaded region represents the scales which Super-CLASS could probe, assuming a one square degree field of view and a source density sufficient to bin galaxies in pixels of one square arcmin.

less efficient at removing gas from the deeper potentials. As a result, more gas stays in the haloes and it is likely this is the cause of the slight discrepancy seen in Fig. 2.

The bottom panel shows the equivalent plot at small scales $k_4 = 40 h/\text{Mpc}$, where we can say in general that the increase in power due to cooling baryons falling into potential wells is less severe for the more overdense regions. This is likely related to the presence of more massive haloes but may also be due to the longer cooling time of the hotter gas associated with these haloes, as well as the increased AGN feedback.

3.3 Comparing the Effect of Baryons with Super-Cluster Selection

In the previous two sub-sections we have looked at how the matter power spectrum is affected by baryons and selection separately. In this section we will compare the two effects, specifically to determine which of the two is more important.

Plotted in Fig. 8 are the median power spectra measured in the HYDRO super-cluster, HYDRO random, DMO super-cluster and DMO random re-simulations divided by the median power spectrum of the DMO random re-simulations, shown by the blue, red, black dash-dotted and black dashed curves respectively. Dividing the median power spectra by that of the DMO random re-simulations, allows us to compare the effect of baryons and selection simultaneously.

Again the shaded area surrounding the curves represent the region between their 16th and 84th percentiles.

On the largest scales, as we showed previously, there is little to no effect on the power spectrum that results from baryons, as the distribution of baryons trace that of the dark matter. In contrast, the power of the super-cluster sample is over double that of the random sample. The super-cluster selection effect boosts the matter power spectrum and is dominant, down to scales $k \sim 5 h/\text{Mpc}$, over the opposing effect of the baryons which suppresses the power.

The blue curve which is the median power spectrum measured from the HYDRO re-simulations of the super-cluster sample, shows which of the two effects is dominant at scales where they oppose each other. It can be seen that on scales between $k \sim 5 - 7 h/\text{Mpc}$ that the baryonic effect starts to dominate. On scales between $k \sim 7 - 20 h/\text{Mpc}$ baryons continue to suppress the power, while the selection effect of the super-cluster sample now switches sign and complements the baryons by further suppressing the power. On these scales both baryonic and selection effects are similar.

On smaller scales, $k \geq 20 h/\text{Mpc}$, the effect of baryons is to boost the power and the suppression of power due to the selection effect begins to dominate again, until $k \sim 50 h/\text{Mpc}$. On scales smaller than this the boost in power from baryons dominates. The shaded grey region shows the scales which we will be able to probe with a weak lensing survey like Super-CLASS. Except for a small range of scales, the selection effect of the super-cluster sample dominates over the effect of baryons.

To summarise, the amount to which the selection effect and baryons affect the matter power spectrum on small scales is similar, but they cancel each other out to a degree. On intermediate scales, which current weak lensing studies can probe, the dominant effect is selection. In addition, we showed in Fig. 5 that the effect of baryons on the matter power spectrum does not vary significantly with redshift. For these reasons, in the next section we will ignore baryonic effects and look at how the more important selection effect of targeting a super-cluster region biases the primary 2-point statistic used in weak lensing surveys, the shear power spectrum.

4 WEAK LENSING SHEAR POWER SPECTRUM

In this section we describe the method we implemented to generate convergence maps along lightcones that intersect our random and super-cluster sub-volumes on the way through the parent simulation. We then examine the effect of selection, i.e. the effect of targeting a super-cluster field as opposed to a random field, on the shear power spectrum by comparing our random and super-cluster convergence maps, before presenting some forecasts for Super-CLASS like weak lensing surveys.

The distortion of a source galaxy, in an image at position $\theta = (\theta_1, \theta_2)$, due to the effect of weak gravitational lensing can be described by two fields. The scalar convergence field $\kappa(\theta)$ describes the change in apparent size of the source galaxy, while the complex valued shear field $\gamma(\theta)$ describes the compression and stretching of the source galaxy. Both of these can be expressed in terms of a lensing potential field

$\psi(\theta)$ as follows,

$$\gamma(\theta) = \gamma_1(\theta) + i\gamma_2(\theta) = \frac{1}{2} \left(\partial_1^2 - \partial_2^2 \right) \psi(\theta) + i\partial_1\partial_2\psi(\theta), \quad (4)$$

$$\kappa(\theta) = \frac{1}{2} \left(\partial_1^2 + \partial_2^2 \right) \psi(\theta), \quad (5)$$

where partial derivatives ∂_1 and ∂_2 are with respect to θ_1 and θ_2 respectively, and γ_1 and γ_2 are the two components of the shear field. Additionally, the convergence field can be related to the projected surface mass density $\Sigma(\theta)$ by

$$\kappa(\theta) = \frac{\Sigma(\theta)}{\Sigma_{\text{crit}}}, \quad (6)$$

where the critical surface mass density is defined by

$$\Sigma_{\text{crit}} = \frac{c^2}{4\pi G} \frac{D_s}{D_l D_{ls}}, \quad (7)$$

where D_{ls} , D_s and D_l are the angular diameter distances from the lens to the source, the observer to the source, and the observer to the lens respectively.

4.1 Convergence and Shear Maps

In section 3 we showed the effect due to measuring the matter power spectrum in a super-cluster sub-volume is more important than the effect of baryonic physics. Additionally, we showed the effect of baryons on the matter power spectrum does not depend greatly on redshift nor the type of sub-volume in which the power spectrum was measured. This leads us to believe the effect of baryons on the matter power spectrum is fairly consistent across a range of different sub-volumes at different redshifts, up to a minimum of $z = 1$. However, given the large effect on the matter power spectrum due to selection, we would also like to examine how much selection biases the shear power spectrum. We went about this by generating convergence maps that targeted our random and super-cluster sub-volumes in the parent simulation.

The convergence in angular pixels was calculated by generating lightcones through our parent simulation, using the method developed in the SUNGLASS pipeline (for more details see, [Kiessling et al. 2011](#)),

$$\kappa_p(r_s) = \sum_k \frac{K(r_k, r_s)}{\Delta\Omega_p \bar{n}(r_k) r_k^2} - \int_0^{r_s} dr K(r, r_s), \quad (8)$$

where $\Delta\Omega_p$ is the pixel area, \bar{n} is the simulation's comoving particle number density, and r_s and r_k are the comoving radial distance to the source plane and position of the k^{th} particle in the lightcone, respectively. The scaled lensing kernel is defined as follows,

$$K(r, r_s) = \frac{3H_0^2 \Omega_m}{2c^2} \frac{(r_s - r)r}{r_s a(r)}. \quad (9)$$

This method exploits the Born approximation to perform a line of sight integration along the unperturbed ray path. This simplification is justified as the effects of lens-lens coupling and higher order corrections of the Born approximation on the convergence power spectrum have been shown to be insignificant on relevant scales (see [Hilbert et al. 2009](#)).

We generated lightcones orientated such that they intersected our super-cluster and random sub-volumes at the

snapshot corresponding to $z = 0.24$, to create one square degree convergence maps with a single source plane at $z = 1$. This was chosen to match the median redshift of the source galaxies estimated in the SKA forecast by [Bonaldi et al. \(2016\)](#). As Super-CLASS has the same frequency, depth and resolution as SKA it will likely have galaxies with a very similar redshift distribution. The angular size of our convergence maps were chosen to match that of the Super-CLASS field. The parent simulation volume was split into equal length sections of comoving distance 400 Mpc along the line of sight, in order to include the evolution of structure. The first 400 Mpc section used was from the snapshot corresponding to $z = 0.05$, this was set up so that the time it takes light to travel from the centre of the section to the start of the lightcone is equal to how much time has passed from $z = 0.05$ to now. All particles that fell within the lightcone's volume were added to the line of sight integration, before adding the next section of the lightcone from the next snapshot. This continued until the snapshot that corresponds to $z = 0.85$ where the lightcone reached the end of the parent simulation volume at 3200 Mpc. As the parent simulation has continuous boundary conditions the next section was naturally taken from the opposite side from the final snapshot corresponding to redshift $z = 1.0$. The particles were binned into a 600^2 grid of pixels, with each square pixel having an area $A = 0.01$ arcmin².

Once the convergence maps were generated, we calculated shear maps in Fourier space using the following relations,

$$\hat{\gamma}_1(\ell) = \frac{\ell_1^2 - \ell_2^2}{\ell_1^2 + \ell_2^2} \hat{\kappa}(\ell), \quad (10)$$

$$\hat{\gamma}_2(\ell) = \frac{2\ell_1\ell_2}{\ell_1^2 + \ell_2^2} \hat{\kappa}(\ell), \quad (11)$$

where ℓ_1 and ℓ_2 are the Fourier conjugates of θ_1 and θ_2 , $\hat{\kappa}$ is the Fourier transform of the convergence, and $\hat{\gamma}_1$ and $\hat{\gamma}_2$ are the Fourier transforms of the two components of the shear.

The left panel of Fig. 10 shows one example of a convergence and shear map taken from our super-cluster sample. The integrated convergence field up to $z = 1$ is shown by the background colour, where the yellow and dark blue regions indicate overdense and underdense areas respectively. The shear field is shown by the white ticks and can be seen to tangentially trace the overdense areas as expected.

4.2 Effect of Super-Cluster Selection on the Convergence Power Spectrum

In this section we present our results for the effect of super-cluster selection on the convergence power spectrum. The convergence and shear power spectra, radially binned in $\ell = (\ell_1^2 + \ell_2^2)^{1/2}$, can be determined from the convergence and shear fields respectively using

$$C_\ell^{\kappa\kappa} = \left(\frac{L}{N} \right)^2 \sum_{\ell \text{ in shell}} \langle |\hat{\kappa}|^2 \rangle, \quad (12)$$

$$C_\ell^{\gamma\gamma} = \left(\frac{L}{N} \right)^2 \sum_{\ell \text{ in shell}} \langle |\hat{\gamma}_1|^2 \rangle + \langle |\hat{\gamma}_2|^2 \rangle, \quad (13)$$

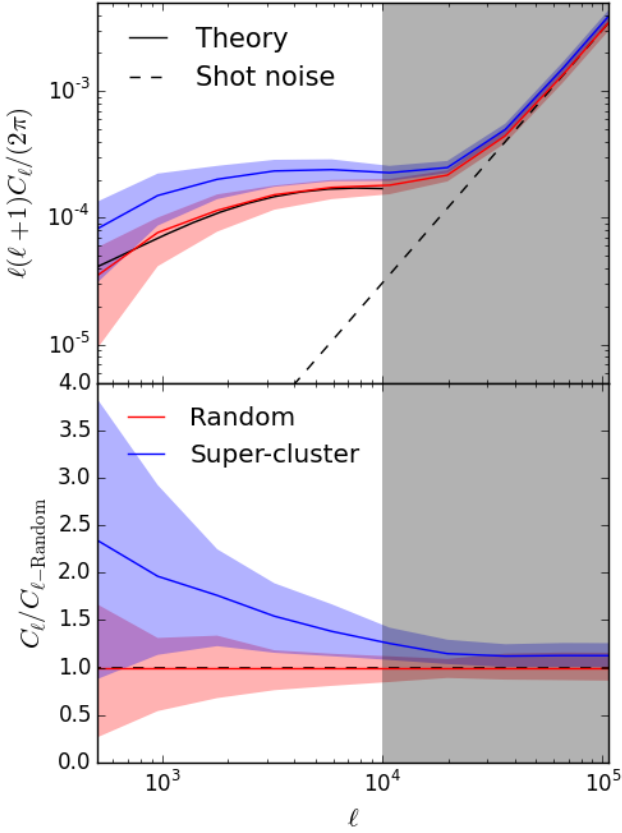


Figure 9. The top panel shows the convergence power spectra of the random and supercluster samples, in red and blue respectively. The shaded areas surrounding the two curves represent the region between their 16th and 84th percentiles. The smooth black curve is the predicted theoretical convergence power spectrum from NICAEA, while the diagonal black dashed line shows the shot noise term. In the bottom panel we plot the convergence power spectra of the random and supercluster samples divided by the median convergence power spectrum of the random sample. The grey shaded region in both panels show the scales for which the measured power spectra begin to be dominated by shot noise.

where L is the angular size of the image field in radians and N is the number of pixels in the image. Here we use angle brackets to refer to the mean of a variable. We calculated the convergence power spectrum for every realization in the two samples. When measuring the power spectrum from a simulation with finite particles we measure $C_\ell^m = C_\ell^{\kappa\kappa} + C_\ell^{SN}$, the desired power spectrum with an additional shot noise component which can be modelled as

$$C_\ell^{SN} = \left(\frac{3H_0^2 \Omega_m}{2c^2} \right)^2 \int_0^{r_s} \frac{(r_s - r)^2}{\bar{n}(r)r_s^2 a(r)^2} dr. \quad (14)$$

The mean 3D number density of particles in the simulation $\bar{n}(r)$, will be constant in comoving coordinates.

The top panel of Fig. 9 shows the median convergence power spectra for our random and super-cluster samples in red and blue respectively, where again the shaded area surrounding the curves represent the region between their 16th and 84th percentiles. We used the publicly available code

NICAEA⁷ (Kilbinger et al. 2009) to predict the theoretical convergence power spectrum, shown by the black curve, assuming the revised HALOFIT (Takahashi et al. 2012) model for the input non-linear matter power spectrum. The shot noise power spectrum is shown by the dotted black line. The median convergence power spectrum of the random sample shows good agreement with the theoretical power spectrum on the scales for which it is predicted. On smaller scales, shaded in grey ($\ell > 10^4$), the measured power spectra begins to be dominated by shot noise.

The bottom panel shows the power spectra of the random and super-cluster samples divided by the median power spectrum of the random sample. This lets us see the effect of selection on the convergence power spectra over a range of scales. We see that on the largest scales the median convergence power spectrum for the super-cluster sample is over twice as large as that for the random sample. On smaller scales, $\ell \sim 10^4$, the super-cluster sample still has approximately 50 percent more power than the random sample. Although we cannot directly compare the matter power spectrum results with these, we can see similarities here with the results of Fig. 3. The boost in power at high ℓ values is likely due to contributions from lower k modes at higher redshifts.

Here we only show the results for the convergence field with a source plane at $z = 1$. However, the same method was used to generate convergence fields at 20 source redshift planes separated by $\Delta z = 0.1$, from $z = 0.1$ to $z = 2$. The median convergence power spectrum for the super-cluster sample is larger than that of the random sample in all slices with redshifts higher than that of super-cluster (i.e. $z \geq 0.3$). At the largest scale the median convergence power spectrum for the super-cluster sample range between 1.7 times and 2.7 times larger than that of random sample, for $z = 2.0$ and $z = 0.5$ respectively.

The minimum ℓ value is limited by the size of our field of view and can be estimated using $\ell_{\min} \sim \pi/\theta_{\text{FOV}} = 180$, where $\theta_{\text{FOV}} = 1$ degree is the angular size of the field of view. In lensing surveys, the maximum ℓ value is limited by the angular size of the pixels θ_{pix} in which you are able to bin a sufficient number of galaxies, i.e. $\ell_{\max} \sim \pi/\theta_{\text{pix}}$. In the Super-CLASS survey we expect θ_{pix} to be around one arcmin, which means $\ell_{\max} \sim 10^4$. Therefore, the approximate range of scales most relevant to this work is, $180 < \ell < 10^4$.

4.3 Forecasts for the Super-CLASS Survey

In the previous sub-section we found that the amplitude of the convergence power spectrum measured from a lightcone which intersects a super-cluster sub-volume is larger on all scales than the equivalent for a random sub-volume. The motivation for this study was to use simulations to forecast the constraining power of the Super-CLASS survey. In this section we add noise to our shear fields, in order to estimate how well we will be able to measure the shear power spectrum from the Super-CLASS radio data.

There are other systematics and sources of bias that can influence shear power spectrum constraints, e.g. galaxy shape and redshift measurements. In addition, certain systematics will affect cosmic shear measurements differently

⁷ <http://www.cosmostat.org/software/nicaea/>

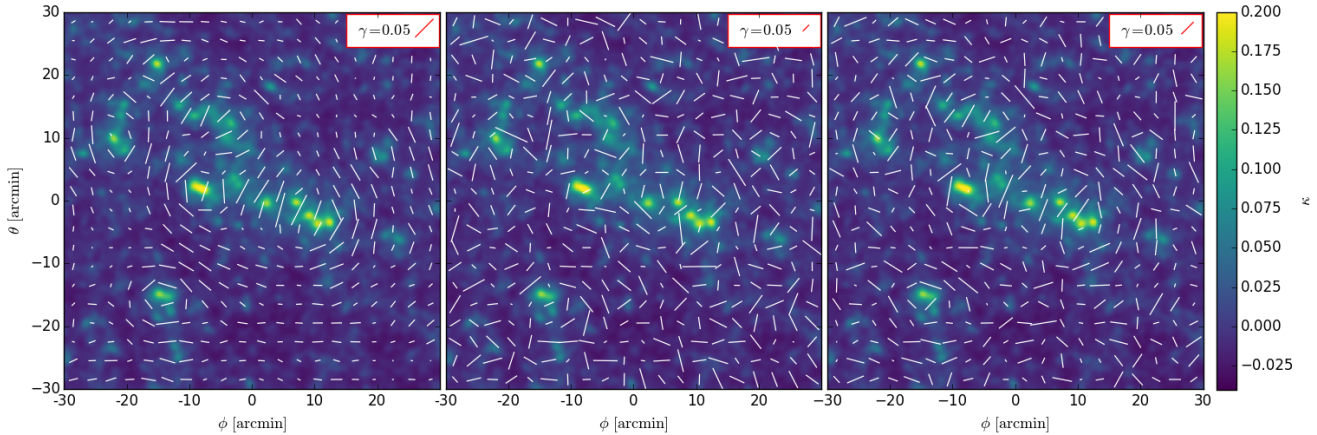


Figure 10. All three panels show one square degree, convergence and shear maps for one member of our super-cluster sample. The background and colour bar show the convergence map, while the white ticks show the shear field. In the left panel the shear ticks represent the shear field before adding noise, while the middle and right panels show the shear fields after adding noise typical of current radio and optical weak lensing surveys, respectively.

in radio and optical weak lensing surveys, e.g. the stability of the telescope beam in the radio band is advantageous as it is almost unaffected by seeing. The main physical systematic is a correlation in the ellipticities of galaxies prior to lensing, i.e. intrinsic alignments. However, nulling techniques and methods in which galaxy pairs are weighted based on their spatial separation can be used to reduce the impact of intrinsic alignments on the measured power. These methods require the redshift distribution of the source galaxies in the survey, which Super-CLASS will include. In addition, redshift measurements could also be used to ensure galaxies that are physically associated with the lens are excluded from the source catalog, in order to reduce the boost factor (Miyatake et al. 2015), which dilutes the signal. We will not investigate the effects of these systematics here as they will be addressed in forthcoming Super-CLASS papers.

When observational data collected from weak lensing surveys is used to investigate cosmic shear, shape measurements of the galaxies are used to estimate the shear. The estimated shear is determined by binning a finite number of galaxies into pixels, before taking the average of their ellipticities. To simulate the associated shape noise we added Gaussian noise to both components of the shear in real space as follows,

$$\gamma_1^i(\theta) = \gamma_1(\theta) + N_1(\theta), \quad (15)$$

$$\gamma_2^i(\theta) = \gamma_2(\theta) + N_2(\theta), \quad (16)$$

where $\gamma_1^i(\theta)$ and γ_2^i are the noisy shear components, and N_1 and N_2 are the added noise fields. Both noise fields were generated with zero mean and a standard deviation, $\sigma_n = \sigma_\epsilon / N_p^{1/2}$, where $N_p = N_a A$ is the number of galaxies per pixel, N_a is the number of galaxies per arcmin², and σ_ϵ is the rms of the typical intrinsic ellipticity. We have taken $\sigma_\epsilon = 0.3/\sqrt{2}$ which is typical of current ground based surveys.

The middle and right panel of Fig. 10 show two shear fields with added noise. We used a source density that is expected for the Super-CLASS radio survey, $N_a^R = 1.5$ galaxies/arcmin², for the middle panel. For the right panel

we used a source density that is typical of high quality ground based optical surveys, $N_a^O = 10$ galaxies/arcmin². The integrated convergence map up to $z = 1$ is shown by the background and colour bar, and is the same in all three panels. The impact of adding noise is largest for the radio scenario, the middle panel. The shear ticks no longer tangentially trace the high convergence regions perfectly, as they do in the left panel. In the optical scenario, the right panel, the shear ticks trace the high convergence regions tangentially fairly well. It is in the low convergence regions where the effect of noise is strongest.

To investigate the effect of noise quantitatively we examine the shear power spectra recovered from the simulations. The shear is a spin-2 field and can be decomposed into gradient (E) and curl (B) components. The scalar potential, from which the shear field arises, only produces E modes. Systematic effects and shape noise present in weak lensing surveys produce both E and B modes. As a result, the B modes can be utilised to test for these effects. As an example, if we were to take the E and B components of our shear field before adding noise, we would find no B component and the E component would be the original convergence field. The result is not as trivial for our noisy shear field. In the Fourier domain we can determine the E component of the shear field $\hat{\gamma}^E(\ell)$ and the B component of the shear field $\hat{\gamma}^B(\ell)$ using the following relations,

$$\hat{\gamma}^E(\ell) = \frac{\ell_1^2 - \ell_2^2}{\ell_1^2 + \ell_2^2} \hat{\gamma}_1^i(\ell) + \frac{2\ell_1\ell_2}{\ell_1^2 + \ell_2^2} \hat{\gamma}_2^i(\ell), \quad (17)$$

$$\hat{\gamma}^B(\ell) = \frac{2\ell_1\ell_2}{\ell_1^2 + \ell_2^2} \hat{\gamma}_1^i(\ell) - \frac{\ell_1^2 - \ell_2^2}{\ell_1^2 + \ell_2^2} \hat{\gamma}_2^i(\ell). \quad (18)$$

The power spectra of the E and B modes, radially binned in $\ell = (\ell_1^2 + \ell_2^2)^{1/2}$, can be calculated using

$$C_\ell^{EE} = \left(\frac{L}{N}\right)^2 \sum_{\ell \text{ in shell}} \left\langle |\hat{\gamma}^E|^2 \right\rangle, \quad (19)$$

$$C_\ell^{BB} = \left(\frac{L}{N}\right)^2 \sum_{\ell \text{ in shell}} \left\langle |\hat{\gamma}^B|^2 \right\rangle, \quad (20)$$

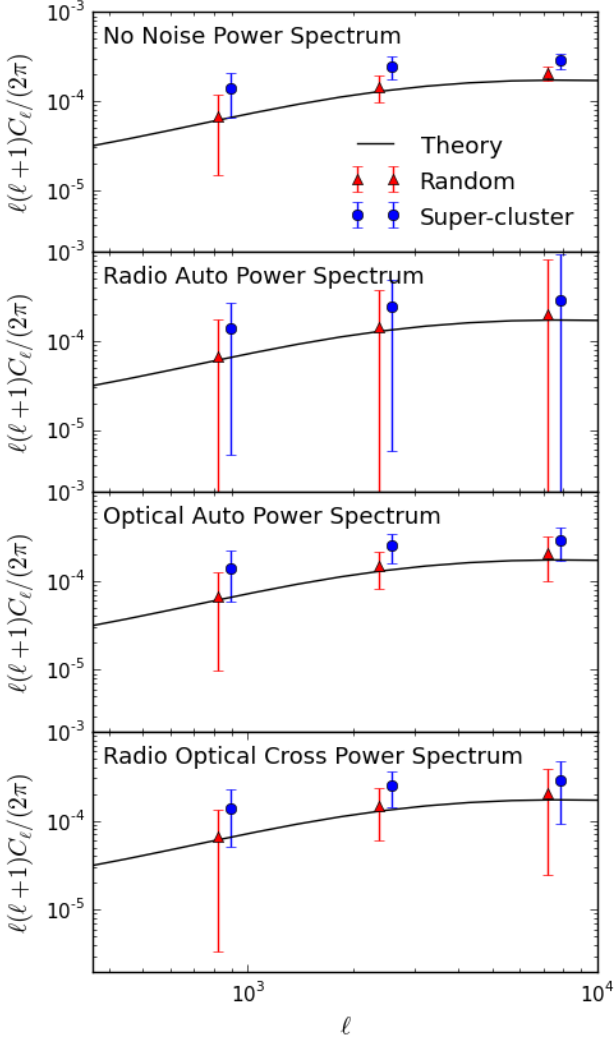


Figure 11. Mean shear power spectra of the random and super-cluster samples are shown in red and blue respectively. The top panel shows the power spectra before adding noise. The second, third and fourth panel from the top show the radio auto power spectrum, the optical auto power spectrum and the radio optical cross power spectrum respectively. The method used to determine the error bars is described in the text.

where L is the angular size of the image field in radians and N is the number of pixels in the image.

The shear field generated from our simulations can only produce E modes. Therefore, the E mode power spectrum contains a signal plus the added noise component. The B mode power spectrum traces the noise component and can be used to estimate the noise bias. We subtracted the mean B mode power spectrum from the E mode power spectra $\hat{C}_l^{EE} = \tilde{C}_l^{EE} - \langle \tilde{C}_l^{BB} \rangle$, for both the random and super-cluster samples, and their mean values are plotted in red and blue respectively in Fig. 11. The shear power spectrum with no noise is shown in the top panel.

The Super-CLASS survey is expected to make shear estimates using overlapping radio and optical observations.

As a result, we forecast the constraining power of the Super-CLASS survey for both optical and radio galaxy source densities. In the second panel down we show the radio auto power spectrum, for which we have used the source density expected for Super-CLASS, $N_a^R = 1.5$ galaxies/arcmin². For the optical auto power spectrum plotted in the third panel down, we used a source density typical of high quality ground based optical surveys, $N_a^O = 10$ galaxies/arcmin². The only difference between these two auto power spectra are the source densities (noise levels) chosen. Note that we are ignoring the possibility that the source density in a super-cluster region could differ to that in a random region. It is likely that fewer source galaxies would be observed in a super-cluster region due to obscuration by the foreground clusters. On the other hand the effect of magnification, which would allow fainter sources to be observed, may counteract this to some degree. For this analysis we do not consider these issues and assume the same source galaxy densities for both the random and super-cluster samples. Plotted in the bottom panel is the radio optical cross power spectrum. The solid black curve plotted in all four panels is the theoretical prediction from NICA EA again. We calculated the error bars using

$$\sigma_l = \sqrt{\langle (\hat{C}_l^{EE})^2 \rangle - \langle \hat{C}_l^{EE} \rangle^2}, \quad (21)$$

where the angle brackets indicate the average taken over our suite of simulations (i.e. our super-cluster or random sample).

The signal to noise S/N , the precision with which the cosmic shear signal can be measured, was determined for the random and super-cluster samples using

$$S/N = \sqrt{\sum_l \left(\frac{\hat{C}_l^{EE}}{\sigma_l} \right)^2}. \quad (22)$$

Additionally, the detection significance D , the significance with which a non zero signal can be detected, was calculated as follows,

$$D = \sqrt{\sum_l \left(\frac{\hat{C}_l^{EE}}{\sigma_l'} \right)^2}, \quad (23)$$

where

$$\sigma_l' = \sqrt{\langle (\hat{C}_l^{BB})^2 \rangle - \langle \hat{C}_l^{BB} \rangle^2}, \quad (24)$$

and $\hat{C}_l^{BB} = \tilde{C}_l^{BB} - \langle \tilde{C}_l^{BB} \rangle$. The signal to noise depends on both the shape noise and the sample variance, while the detection significance depends solely on the former. The signal to noise and detection significance for all four scenarios are shown in Table 2, the errors represent the 16th and 84th percentiles of the distribution. Note all values displayed in Table 2 are the mean over one thousand realizations of the noise and do not take into account any systematic effects.

The error bars in the first scenario, in which no shape noise was added to the shear field, for both the signal to noise values and the shear power spectrum are entirely due to sample variance. This provides us with an idealised scenario, which we can compare the effect of varying shape noise to. We found that the signal to noise and detection significance in the three noise scenarios are higher for the super-cluster

Table 2. Median signal to noise and detection significance values of the random and super-cluster samples for varying source densities in the absence of systematic effects. The error bars shown represent the 16th and 84th percentiles of the respective sample's distribution.

Power Spectrum	Source Density galaxies/armin ²	Random S/N	Random D	Super-cluster S/N	Super-cluster D
No Noise	∞	$6.5^{+1.2}_{-1.4}$	∞	$6.3^{+1.5}_{-1.3}$	∞
Radio Auto	1.5	$1.7^{+0.9}_{-0.7}$	$2.0^{+1.0}_{-0.9}$	$2.0^{+1.1}_{-0.8}$	$2.7^{+1.5}_{-1.2}$
Optical Auto	10	$3.3^{+1.1}_{-1.0}$	$7.4^{+3.2}_{-2.3}$	$4.1^{+1.4}_{-1.1}$	$13.7^{+8.0}_{-4.7}$
Radio Optical Cross	1.5, 10	$2.5^{+1.0}_{-0.8}$	$4.4^{+2.0}_{-1.6}$	$3.3^{+1.3}_{-1.0}$	$7.6^{+4.6}_{-2.7}$

sample than they are for the random sample. This is due to the amplitude of the convergence power spectrum of the super-cluster sample being larger than that of the random sample, as was shown in Fig. 9.

We should reiterate that the following results ignore all systematic effects. The simulated radio data has a detection significance of $2.7^{+1.5}_{-1.2}$ for the super-cluster sample, which is likely high enough to make a cosmic shear detection. The difference between surveying a super-cluster region as opposed to a random region, could make a cosmic shear detection possible, assuming the source galaxy density predicted for Super-CLASS is achieved. This was indeed the reasoning for an overdense super-cluster region of the sky to be chosen as the target of the Super-CLASS field.

As is to be expected, the third panel of the figure and row of the table show a more promising scenario for a source density typical of ground based optical surveys. In this case both the signal to noise and detection significance are sufficient for a cosmic shear detection, even in the random sample.

In the bottom panel and row, the optical radio cross power spectrum is seen to be a significant improvement on the radio auto power spectrum. The overlapping radio and optical observations when cross correlated produce a detection significance of $7.6^{+4.6}_{-2.7}$, which is a strong cosmic shear detection.

5 SUMMARY AND CONCLUSIONS

The radio weak lensing survey Super-CLASS aims to measure the cosmic shear signal by targeting an overdense region of the sky that contains five Abell clusters. Two issues that are relevant to the detection of this signal are the effect of selection and the impact of baryons on the matter distribution. We have investigated both issues in this paper by identifying a sample of super-cluster and random sub-volumes from a large dark matter only (parent) simulation. These sub-volumes were re-simulated, using zoom techniques, at a higher resolution and with full gas physics. This enabled us to examine the effect of baryons on the matter power spectrum in these sub-volumes along with the aforementioned selection effect. We also generated shear and convergence maps using the line of sight integration technique, which intercept the random and supercluster regions at $z = 0.24$. These were then used to study the difference between the shear power spectra measured by a weak lensing survey that targets a random patch of the sky as opposed to one containing a super-cluster. Our key results are summarised as follows:

- On large scales ($k \leq 1 h/\text{Mpc}$) the matter power spectrum measured from our super-cluster sample has at least twice as much power as that measured from the random sample (Fig. 3). Meanwhile, on small scales ($k \geq 10 h/\text{Mpc}$), the power in the super-cluster sample is less than 90% of the random sample. We then took all members of the two samples and found that a correlation exists between the overdensity in a sub-volume and the amplitude of the matter power spectrum at different scales. In Fig. 4, we showed that on large scales ($k = 1 h/\text{Mpc}$) sub-volumes with higher overdensity generally had a higher amplitude, whilst on small scales ($k \leq 50 h/\text{Mpc}$) higher overdensity sub-volumes had a lower amplitude.

- Our investigation of the effects of baryonic physics on the matter power spectrum in our random sample are broadly consistent with previous studies (e.g., van Daalen et al. 2011). On intermediate scales ($k = 1 - 10 h/\text{Mpc}$) the HYDRO matter power spectrum is suppressed by $\sim 10\%$ in comparison to that of the DMO, while on small scales ($k \geq 30 h/\text{Mpc}$) it is boosted considerably. In addition, we found that the effect of baryonic physics on the matter power spectrum does not change significantly between $z = 0$ and $z = 1$ (Fig. 5). We did find that there is a significant, although very small, difference in the effect of baryons on the matter power spectrum between our super-cluster and random sample. In general, the effect of baryons on the matter power spectrum on all scales is suppressed more when the sub-volume from which it is being measured is more overdense (Figs. 5, 6 and 7).

- We compared the selection effect with the baryonic effect on the matter power spectrum in Fig. 8. On large scales, specifically for $k \leq 5 h/\text{Mpc}$, the effect of selection dominates over the effect of baryons, boosting the power. On smaller scales than this, the two effects go back and forth between complementing and competing with one another. However, the selection effect is dominant, particularly on scales relevant for radio weak lensing studies.

- Next we studied the effect on the weak lensing convergence power spectrum that results from targeting super-cluster regions when generating lightcones through the parent simulation. We found that the convergence power spectrum measured in our super-cluster sample had more power on all scales measured, than that of our random sample. More specifically, for $\ell > 10^3$ the amplitude of the convergence power spectra for the super-cluster sample was twice that of the random sample (Fig. 9).

- Finally, we made some forecasts for Super-CLASS like weak lensing surveys and optical surveys using the same field of view and higher galaxy source densities. We found that targeting a super-cluster region as opposed to a random re-

gion, with the source density expected for the Super-CLASS project, generates a detection significance of $2.7^{+1.5}_{-1.2}$. This indicates that in the absence of systematic effects the Super-CLASS project will likely make a cosmic shear detection. In addition, the radio optical cross power spectra generates a detection significance of $7.6^{+4.6}_{-2.7}$, therefore cross correlating with an optical survey would guarantee a cosmic shear detection provided systematics can be adequately corrected for (Fig. 11 and Table 2).

To conclude, although the effect of baryons on the matter power spectrum found are important to take into account in future weak lensing surveys, they are not a concerning systematic for the Super-CLASS project. On scales relevant for radio surveys like Super-CLASS the selection effect is most important, i.e. the effect of targeting a super-cluster field, which boost the amplitude of the matter and shear power spectrum considerably. Finally, we showed using simulations that the Super-CLASS project's method of targeting a super-cluster region of the sky, should allow for a cosmic shear detection to be made assuming systematics can be corrected for.

ACKNOWLEDGEMENTS

We would like to thank Ian McCarthy for providing the BAHAMAS data and code, used to create our hydrodynamic simulations. We also thank Adrian Jenkins for providing the initial conditions code used in the MACSIS project. STK and DJB acknowledge support from STFC through grant ST/L000768/1. AP and MLB were supported by an ERC Starting Grant (grant no. 280127).

This work used the DiRAC Data Centric system at Durham University, operated by the Institute for Computational Cosmology on behalf of the STFC DiRAC HPC Facility (www.dirac.ac.uk). This equipment was funded by BIS National E-infrastructure capital grant ST/K00042X/1, STFC capital grants ST/H008519/1 and ST/K00087X/1, STFC DiRAC Operations grant ST/K003267/1 and Durham University. DiRAC is part of the National E-Infrastructure.

REFERENCES

Abbott T., et al., 2016, *Phys. Rev. D*, 94, 022001
 Barnes D. J., Kay S. T., Henson M. A., McCarthy I. G., Schaye J., Jenkins A., 2017, *MNRAS*, 465, 213
 Bartelmann M., Schneider P., 2001, *Phys. Rep.*, 340, 291
 Benjamin J., et al., 2013, *MNRAS*, 431, 1547
 Bonaldi A., Harrison I., Camera S., Brown M. L., 2016, preprint ([arXiv:1601.03948](https://arxiv.org/abs/1601.03948))
 Booth C. M., Schaye J., 2009, *MNRAS*, 398, 53
 Briel U. G., Henry J. P., 1993, *A&A*, 278, 379
 Brown M. L., Battye R. A., 2011, *MNRAS*, 410, 2057
 Brown M. L., Taylor A. N., Bacon D. J., Gray M. E., Dye S., Meisenheimer K., Wolf C., 2003, *MNRAS*, 341, 100
 Brown M. L., et al., 2015, *PoS, AASKA14*, 023
 Casarini L., Macciò A. V., Bonometto S. A., Stinson G. S., 2011, *MNRAS*, 412, 911
 Chiang C.-T., Wagner C., Schmidt F., Komatsu E., 2014, *JCAP*, 1405, 048
 Colombi S., Jaffe A. H., Novikov D., Pichon C., 2009, *MNRAS*, 393, 511

Dalal N., White M., Bond J. R., Shirokov A., 2008, *ApJ*, 687, 12
 Dalla Vecchia C., Schaye J., 2008, *MNRAS*, 387, 1431
 Davis M., Efstathiou G., Frenk C. S., White S. D. M., 1985, *ApJ*, 292, 371
 Demetroullas C., Brown M. L., 2016, *MNRAS*, 456, 3100
 Dolag K., Borgani S., Murante G., Springel V., 2009, *MNRAS*, 399, 497
 Fu L., et al., 2008, *A&A*, 479, 9
 Fu L., Kilbinger M., Erben T., Heymans C., Hildebrandt H., et al., 2014, *MNRAS*, 441, 2725
 Gray M. E., Taylor A. N., Meisenheimer K., Dye S., Wolf C., Thommes E., 2002, *ApJ*, 568, 141
 Guillet T., Teyssier R., Colombi S., 2010, *MNRAS*, 405, 525
 Hamilton A. J. S., Rimes C. D., Scoccimarro R., 2006, *MNRAS*, 371, 1188
 Harrison I., Camera S., Zuntz J., Brown M. L., 2016, preprint ([arXiv:1601.03947](https://arxiv.org/abs/1601.03947))
 Henson M. A., Barnes D. J., Kay S. T., McCarthy I. G., Schaye J., 2016, preprint ([arXiv:1607.08550](https://arxiv.org/abs/1607.08550))
 Heymans C., et al., 2008, *MNRAS*, 385, 1431
 Heymans C., Grocutt E., Heavens A., Kilbinger M., Kitching T. D., et al., 2013, *MNRAS*, 432, 2433
 Hilbert S., Hartlap J., White S. D. M., Schneider P., 2009, *A&A*, 499, 31
 Hildebrandt H., et al., 2016, preprint ([arXiv:1606.05338](https://arxiv.org/abs/1606.05338))
 Hoekstra H., Jain B., 2008, *Ann.Rev.Nucl.Part.Sci.*, 58, 99
 Jee M. J., Tyson J. A., Schneider M. D., Wittman D., Schmidt S., Hilbert S., 2013, *ApJ*, 765, 74
 Jenkins A., 2010, *MNRAS*, 403, 1859
 Jenkins A., 2013, *MNRAS*, 434, 2094
 Jenkins A., Booth S., 2013, preprint, ([arXiv:1306.5771](https://arxiv.org/abs/1306.5771))
 Jing Y. P., Zhang P., Lin W. P., Gao L., Springel V., 2006, *ApJ*, 640, L119
 Kaiser N., 1992, *ApJ*, 388, 272
 Katz N., White S. D. M., 1993, *ApJ*, 412, 455
 Kiessling A., Heavens A. F., Taylor A. N., Joachimi B., 2011, *MNRAS*, 414, 2235
 Kilbinger M., et al., 2009, *A&A*, 497, 677
 Kilbinger M., et al., 2013, *MNRAS*, 430, 2200
 Lacey C., Cole S., 1994, *MNRAS*, 271, 676
 McCarthy I. G., Schaye J., Bird S., Le Brun A. M. C., 2016, preprint, ([arXiv:1603.02702](https://arxiv.org/abs/1603.02702))
 Miyatake H., et al., 2015, *ApJ*, 806, 1
 Planck Collaboration et al., 2014, *A&A*, 571, A16
 Pratt G. W., Croston J. H., Arnaud M., Boehringer H., 2009, *A&A*, 498, 361
 Rudd D. H., Zentner A. R., Kravtsov A. V., 2008, *ApJ*, 672, 19
 Sadat R., Blanchard A., Kneib J.-P., Mathez G., Madore B., Mazzearella J. M., 2004, *A&A*, 424, 1097
 Schaye J., Dalla Vecchia C., 2008, *MNRAS*, 383, 1210
 Schaye J., et al., 2010, *MNRAS*, 402, 1536
 Schneider P., 2005, [arXiv:astro-ph/0509252](https://arxiv.org/abs/astro-ph/0509252),
 Semboloni E., Hoekstra H., Schaye J., van Daalen M. P., McCarthy I. G., 2011, *MNRAS*, 417, 2020
 Springel V., 2005, *MNRAS*, 364, 1105
 Springel V., White S. D. M., Tormen G., Kauffmann G., 2001, *MNRAS*, 328, 726
 Springel V., et al., 2008, *MNRAS*, 391, 1685
 Takahashi R., et al., 2009, *ApJ*, 700, 479
 Takahashi R., Sato M., Nishimichi T., Taruya A., Oguri M., 2012, *ApJ*, 761, 152
 Tormen G., Bouchet F. R., White S. D. M., 1997, *MNRAS*, 286, 865
 White S. D. M., 1994, [arXiv:astro-ph/9410043](https://arxiv.org/abs/astro-ph/9410043),
 Wiersma R. P. C., Schaye J., Smith B. D., 2009, *MNRAS*, 393, 99
 van Daalen M. P., Schaye J., Booth C. M., Dalla Vecchia C., 2011, *MNRAS*, 415, 3649

This paper has been typeset from a $\text{T}_{\text{E}}\text{X}/\text{L}_{\text{A}}\text{T}_{\text{E}}\text{X}$ file prepared by the author.